Supporting Information

Ag^{1+} Incorporation via Zr^{4+}-Anchored Metalloligand: Fine-Tuning the Single-Atom Catalytic Ag Sites in Zr/Ag Bimetallic Clusters for Enhanced eCO_2RR-to-CO activity

Liang-Jun Li,[a] Wen-Lei Mu,[a] Yi-Qi Tian,[a] Wei-Dong Yu,[b]* Lan-Yan Li,[b]* Jun Yan,[a] and Chao Liu*[a]

a College of Chemistry and Chemical Engineering, Central South University, Changsha 410083, Hunan, P. R. China, E-mail: chaoliu@csu.edu.cn

b China College of Science, Hunan University of Technology and Business, Changsha 410000, Hunan, P. R. China

1. Experimental section

Materials and Instruments All reagents were purchased commercially and were not further purified when used. Powder X-ray difraction (PXRD) analysis were performed on a Rigaku Mini Flex II diffractometer at a 2θ range of 5–50° with Cu Kα radiation. Infrared spectra (KBr) were recorded on Nicolet 6700 spectrometer FT-IR spectrophotometer (Thermo Fisher Scientific, USA). Diffuse reflectance spectra were obtained on UV-4000 spectrophotometer. Electrospray ionization mass spectrometry (ESI-MS) experiments were performed on a Bruker Daltonik GmbH (Bruker, Germany). Photoelectrochemical tests were performed on a CHI 660E electrochemical workstation. X-ray Crystallography data were recorded on a Rigaku XtalAB Synergy DS diffractometer with graphite monochromated Cu Kα radiation. The initial structures are solved by the direct method and refined by the full-matrix least-squares on F2. Details of the structure solution and final refinements are given in Table S1. CCDC 2290841-2290844 contain the supplementary crystallographic data for this paper, which is available freely from the Cambridge Crystallography Data Centre.

Synthesis of Compounds

Synthesis for $[Zr_2Na_2(TC4A)_2(acac)_2]$ $\{Zr_2Na_2\}$: TC4A (30.0 mg,0.04 mmol), $Zr(acac)_4$ (73.15 mmg, 0.15 mmol), squaric acid (H_2Sal) (8.55 mg, 0.075 mmol), and 3 mL acetonitrile (MeCN) were added into a 10 mL glass bottle, 50 μL triethylamine were added dropwise. The solution was sonicated for 5 min, then transferred to an oven at 80℃ for 3 days. Colorless crystals of **Zr_2Na_2** were obtained and washed with MeCN, then dried at room temperature (yield: ~62%).

Synthesis for $[Zr_2Ag_2(TC4A)_2(acac)_2]$ $\{Zr_2Ag_2\}$: TC4A (30.0 mg, 0.04 mmol), $Zr(acac)_4$ (73.2 mmg,0.15 mmol), AgOAc (25.0 mg, 0.15 mmol) and 3 mL of MeCN/DMF (1/1: v/v) were added into a 10 mL glass bottle, 50 μL triethylamine were added dropwise. The solution was sonicated for 5 min, then transferred to an oven at 80℃ for 3 days. Colorless crystals of **Zr_2Ag_2** were obtained and washed with MeCN, then dried at room temperature (yield: ~68%).

Synthesis for $\{H_2ZrAg_3(TC4A)_2(HSal)\}$ $\{$**$ZrAg_3$**$\}$: TC4A (30.0 mg, 0.04 mmol), $Zr(acac)_4$ (73.2 mmg,0.15 mmol), AgOAc (25.0 mg, 0.15 mmol), HSal (69.0 mg, 0.5mmol) and 3 mL of MeCN were added into a 10 mL glass bottle, 50 μL triethylamine were added dropwise. The solution was sonicated for 5 min, then transferred to an oven at 80°C for 3 days. Colorless crystals of **$ZrAg_3$** were obtained and washed with MeCN, then dried at room temperature (yield: ~60%).

Synthesis for $\{HNEt_3\}_2\{H_2Zr_2Ag_7(TC4A)_4(Sal)_2\}$ $4CH_3CN$ $\{Zr_2Ag_7\}$:

Method 1: TC4A (30.0 mg, 0.04 mmol), $Zr(OAc)_4$ (150 µL, 0.5 mmol), CF_3COOAg (30.0 mg, 0.14 mmol), H_2Sal (69.0 mg, 0.5mmol) and 3 mL of MeCN were added into a 10 mL glass bottle, 50 µL triethylamine were added dropwise. The solution was sonicated for 5 min, then transferred to an oven at 80°C for 3 days. Colorless crystals of **Zr_2Ag_7** were obtained and washed with MeCN, then dried at room temperature (yield: ~66%).

Method 2: $ZrAg_3$ (100 mg, 0.05 mmol), H_2Sal (35.0 mg,0.25 mmol) and AgOAc (10 mg, 0.06 mmol) were added into a 25 mL Teflon lined stainless steel autoclave with mixed solvent of MeCN and DCM (3 mL, v:v=5:1). The resulting mixtures were sonicated for 5 min, then were transferred to a preheated oven at 100°C for 3 days. Colorless crystals were obtained after cooling to 25 °C in a yield of ~35% (based on **$ZrAg_3$**).

Scheme S1. Synthetic Routes for **Zr_2Ag_7**.

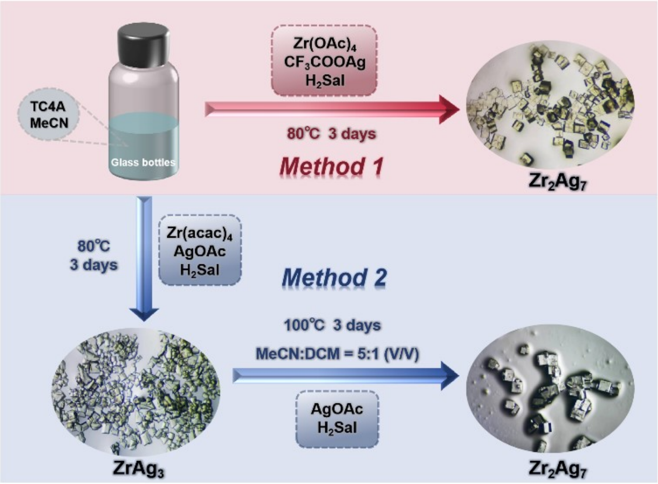

Electrochemical Measurements The electrochemical performance was tested on CHI 660E (Shanghai) electrochemical workstation. All electrochemical measurements were carried out in a gas-tight H-cell separated by Nafion 117 membrane between the two compartments. Each part has 60 ml 0.5 M $KHCO_3$ electrolyte and 40 mL headspace. The test system uses a standard three-electrode system, an Ag/AgCl electrode is used as the reference electrode, carbon rod is the counter electrode, and catalysts modified carbon cloth electrodes were used as the working electrode. 100 µL catalysts suspension (20 wt% loading on acetylene black) and 0.5wt% Nafion solution were dropped on carbon cloth (1×1 cm^2). Before electrolysis measurement of CO_2 reduction, CO_2 was purged into the reaction system. Linear sweep voltammetry (LSV) was performed with a scan rate of 5 mV s^{-1} from 0 V to -1.2 V vs. Ag/AgCl in Ar-saturated and CO_2-saturated conditions. CO_2 atmosphere has been maintained during the testing process at rate of 20 mL/min. Gas phase products was analysis quantitatively using a Shimadzu GC-2014C Gas Chromatograph (Ar as gas carrier).

Computational details. Density functional theory (DFT) calculations are performed with Vienna *ab initio* simulation package (VASP 6.2.1).[1-4.]The Perdew-Burke-Ernzerhof (PBE) functional is applied to describe the electronic exchange-correlation interaction.[5.]The projector augmented-wave (PAW) method is employed to treat core-valence electron interaction.[6.]The convergence criteria are set at 0.05 eV/Å for maximum forces as well as 1×10^{-5} eV for the relative energies. A cutoff energy of 460 eV is adopted for plane-wave basis sets. The lattice parameters of a= 38.3 Å, b= 38.4 Å and c= 38.0 Å are set to avoid the interaction among mirror images. Integration over the Brillouin zone was performed with a reciprocal space mesh consisting of only the Gamma point.[7.]All atoms are allowed to relax during the structural optimization.

Reference

1. Kresse, G.; Joubert, D. From ultrasoft pseudopotentials to the projector augmented-wave method. *Physical Review B* 1999, **59**, 1758-1775.
2. Kresse, G.; Hafner, J. Ab initio molecular dynamics for liquid metals. *Physical Review B* 1993, **47**, 558-561.
3. Kresse, G.; Furthmüller, J. Efficient iterative schemes for ab initio total-energy calculations using a plane-wave basis set. *Physical Review B* 1996, **54**, 11169-11186.
4. Kresse, G.; Furthmüller, J. Efficiency of ab-initio total energy calculations for metals and semiconductors using a plane-wave basis set. Computational *Materials Science* 1996, **6**, 15-50.
5. Perdew, J. P.; Burke, K.; Ernzerhof, M. Generalized Gradient Approximation Made Simple. *Phys. Rev. Lett.* 1996, **77**, 3865-3868.
6. Blöchl, P. E. Projector augmented-wave method. *Physical Review B* 1994, **50**, 17953-17979.
7. Monkhorst, H. J.; Pack, J. D. Special points for Brillouin-zone integrations. *Physical Review B* 1976, **13**, 5188-5192.

2. Structure of Compounds

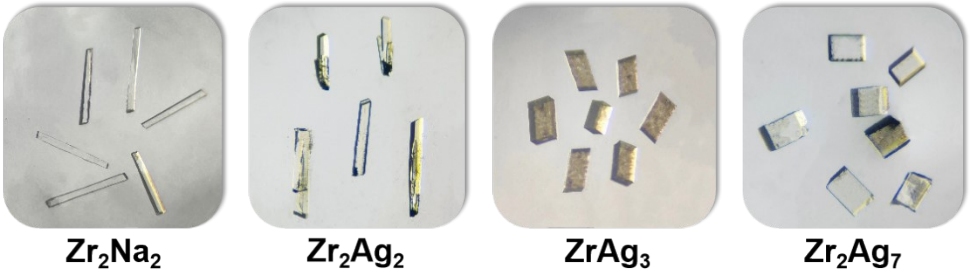

Figure S1. Fresh crystal images of all clusters separated from the solution.

Table S1. X-ray measurements and structure solution of the compounds**.**

Compound	**Zr_2Na_2**	**Zr_2Ag_2**	**$ZrAg_3$**	**Zr_2Ag_7**
CCDC	2290841	2290842	2290843	2290844
Formula	$C_{94}H_{110}N_2Na_2$ $O_{12}S_8Zr_2$	$C_{100}H_{122}Ag_2N_4$ $O_{14}S_8Zr_2$	$Ag_3C_{87}O_{11}S_8ZrH_{92}$	$C_{197}H_{228}Ag_7N_4$ $O_{25}S_{16}Zr_2$
T(K)	293(2)	150	150	150
F_w	1944.73	2258.67	1984.91	4502.31
Crystal system	triclinic	orthorhombic	monoclinic	monoclinic
Space group	P-1	Pbca	$P2_1/n$	$P2_1/n$
a, Å	15.2188(5)	26.4396(2)	21.2954(4)	19.50529(11)
b, Å	19.6877(7)	12.29540(11)	42.6550(9)	36.9188(2)
c, Å	20.5242(6)	32.4346(3)	26.1848(5)	32.66914(16)
α/ °	65.104(3)	90	90	90
β/°	85.720(3)	90	109.152(2)	98.6186((5)
γ/°	69.053(3)	90	90	90
V/Å^3	5188.5(3)	10544.00(15)	22468.6(8)	23259.8(2)
Z	2	4	4	4
ρ_{calcd}/gcm^{-3})	1.245	1.423	1.174	1.286
μ/mm^{-1})	3.668	6.479	4.467	7.114
F(000)	2028.0	4656.0	8088.0	9212.0
2Θ range for data collection/°	5.426 to 153.394	5.45 to 146.13	4.226 to 105.964	3.634 to 145.96
Reflections collected	71680	39225	39326	174967
Data/restraints/parameters	20759/336/1326	9834/169/698	39326/2156/1933	43385/939/2681
Goof	1.013	1.028	1.174	1.074
R_1/wR_2(I>2σ(I))	0.0502/0.1260	0.0354/0.0915	0.1535/0.3093	0.0672/0.1835
R_1/wR_2(all data)	0.0633/0.1372	0.0418/0.0957	0.1801/0.3258	0.0845/0.1947

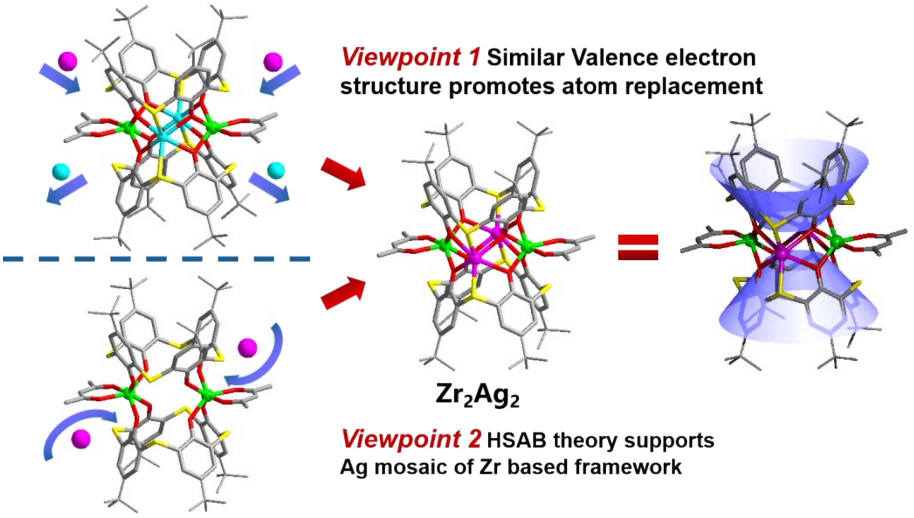

Figure S2. Illustration of the assembly of the **Zr_2Ag_2**.

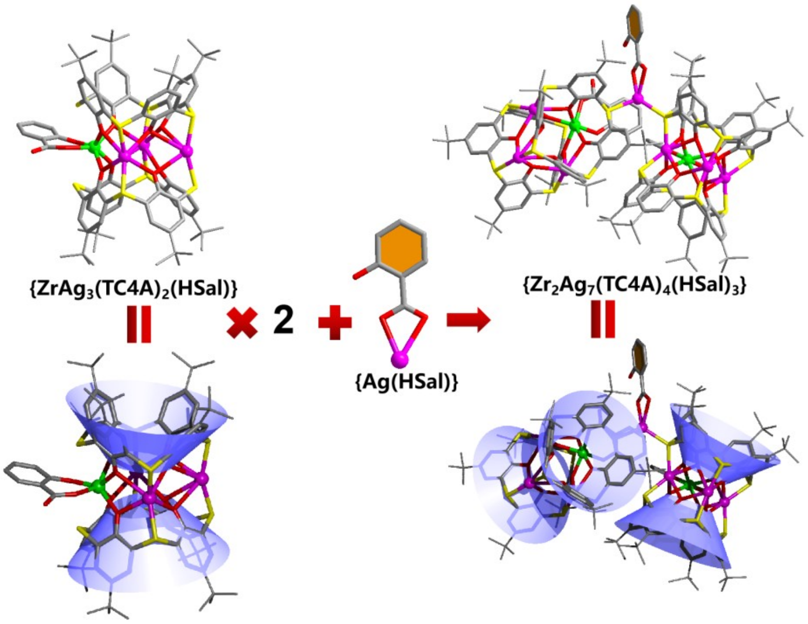

Figure S3. Illustration of the assembly of the **Zr_2Ag_7**.

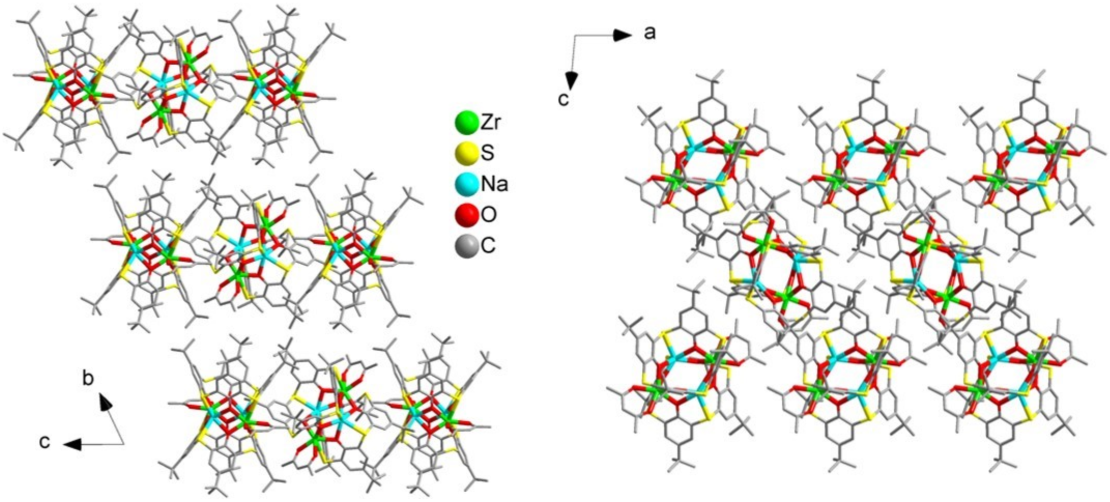

Figure S4. Three-dimensional packing structure of **Zr_2Na_2** along the a and b axis.

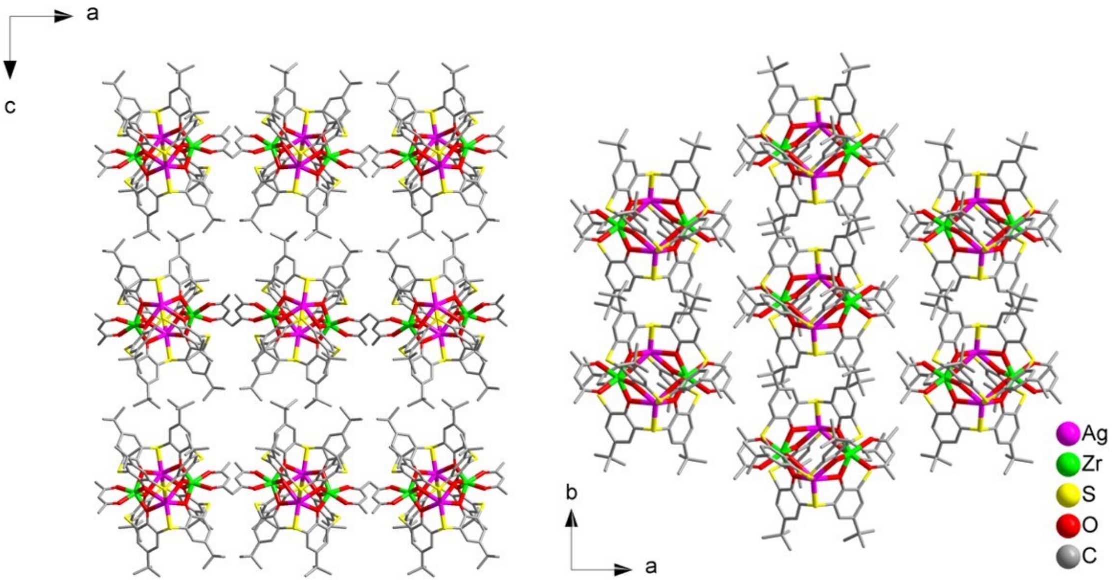

Figure S5. Three-dimensional packing structure of **Zr_2Ag_2** along the b and c axis.

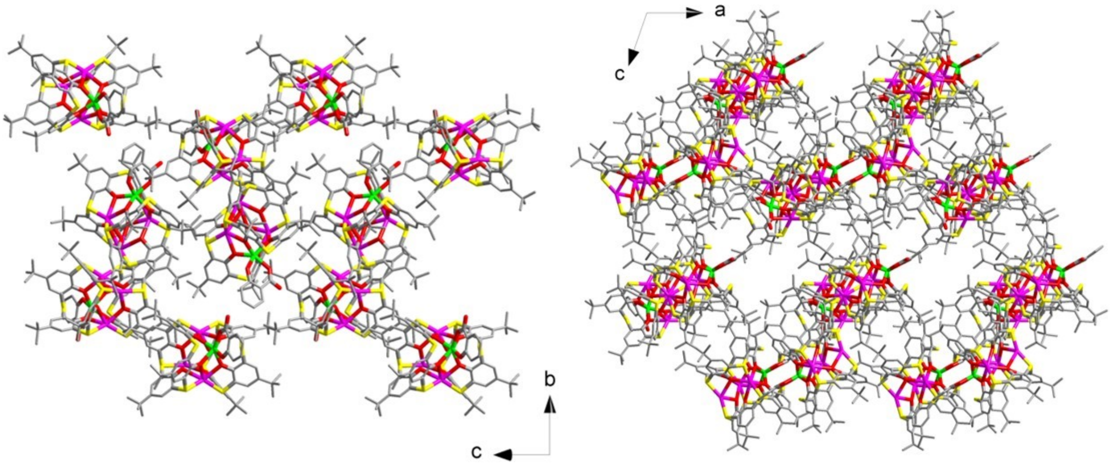

Figure S6. Three-dimensional packing structure of **$ZrAg_3$** along the a and b axis.

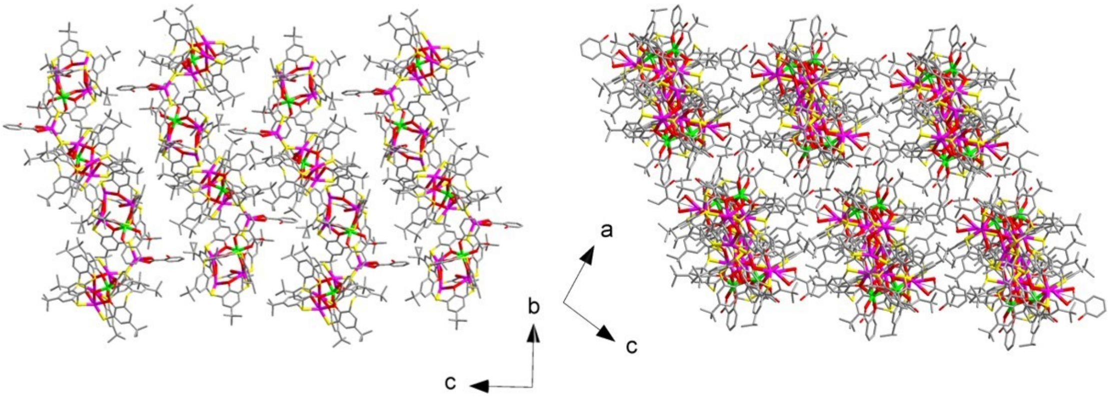

Figure S7. Three-dimensional packing structure of **Zr_2Ag_7** along the a axis.

2. Powder X-ray diffraction

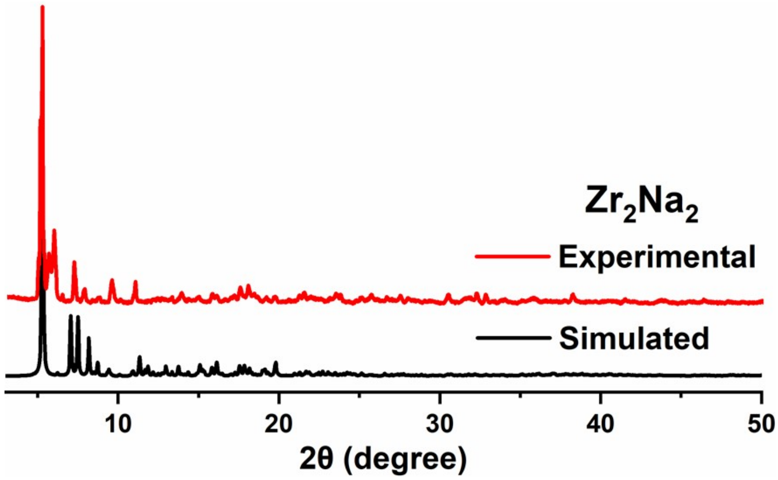

Figure S8. The XRD pattern of **Zr_2Na_2**.

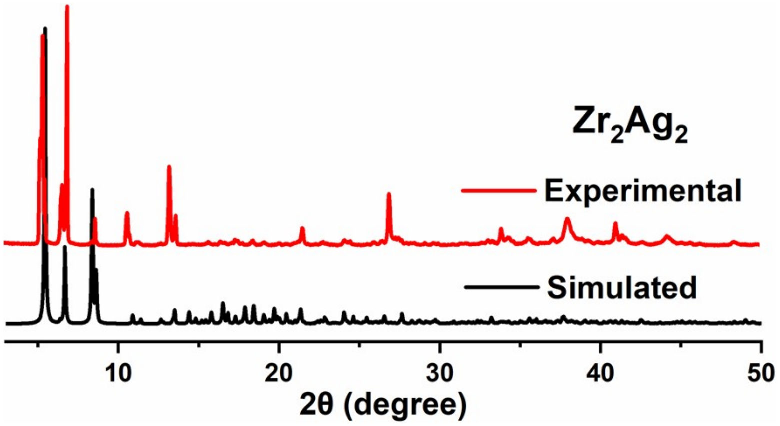

Figure S9. The XRD pattern of **Zr_2Ag_2**.

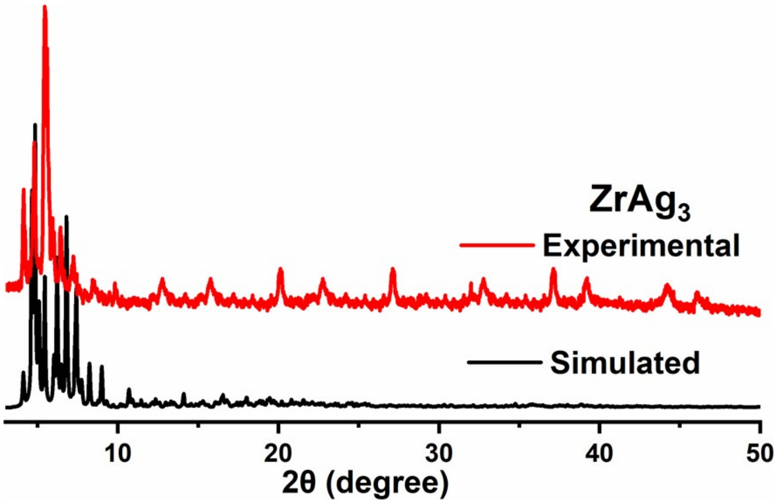

Figure S10. The XRD pattern of **$ZrAg_3$**.

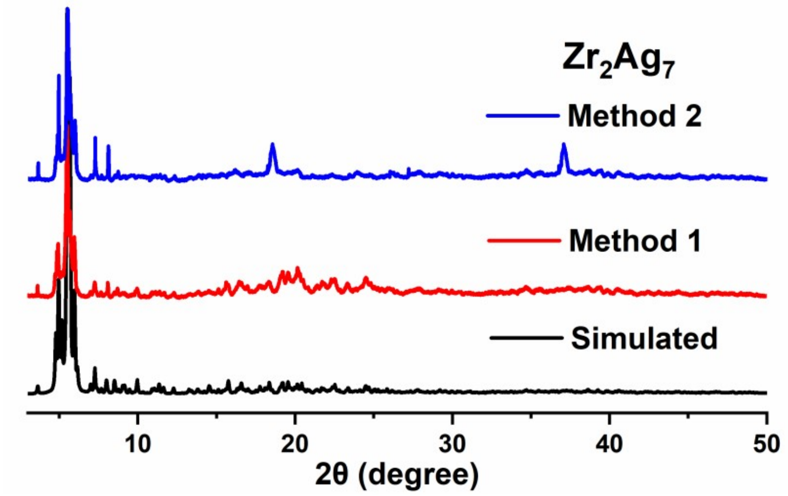

Figure S11. The XRD patterns of **Zr_2Ag_7** obtained under different synthesis methods.

4. FT-IR spectra

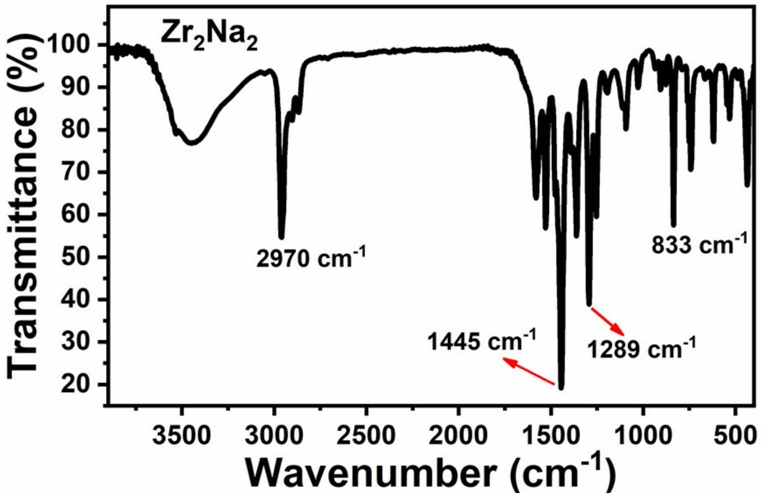

Figure S12. IR spectrum of crystal sample of **Zr_2Na_2**.

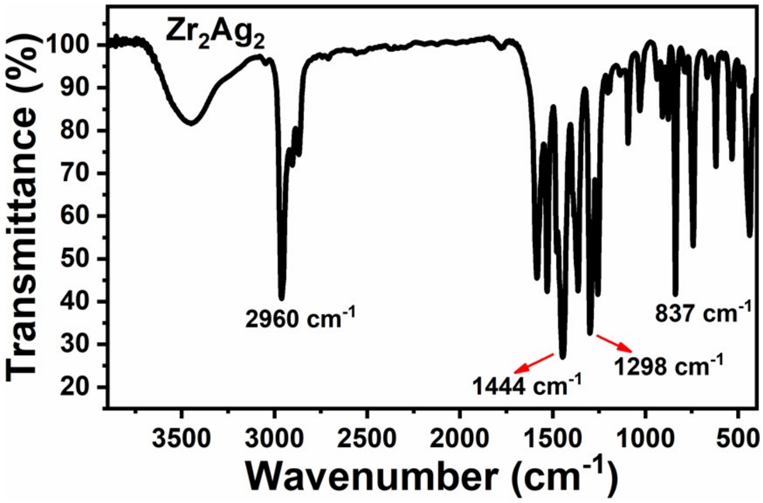

Figure S13. IR spectrum of crystal sample of **Zr_2Ag_2**.

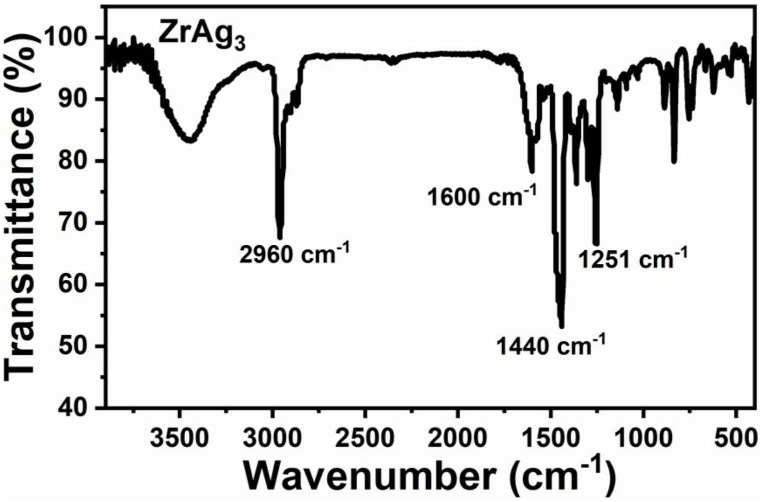

Figure S14. IR spectrum of crystal sample of **ZrAg$_3$**.

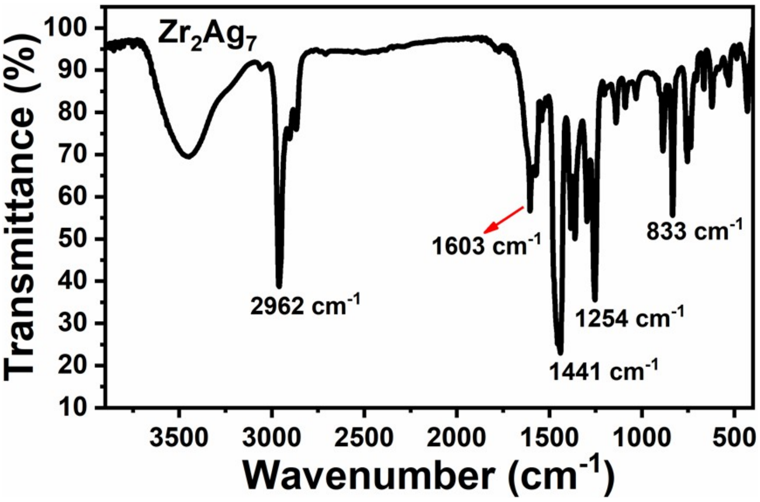

Figure S15. IR spectrum of crystal sample of **Zr$_2$Ag$_7$**.

5. TG-Measurement

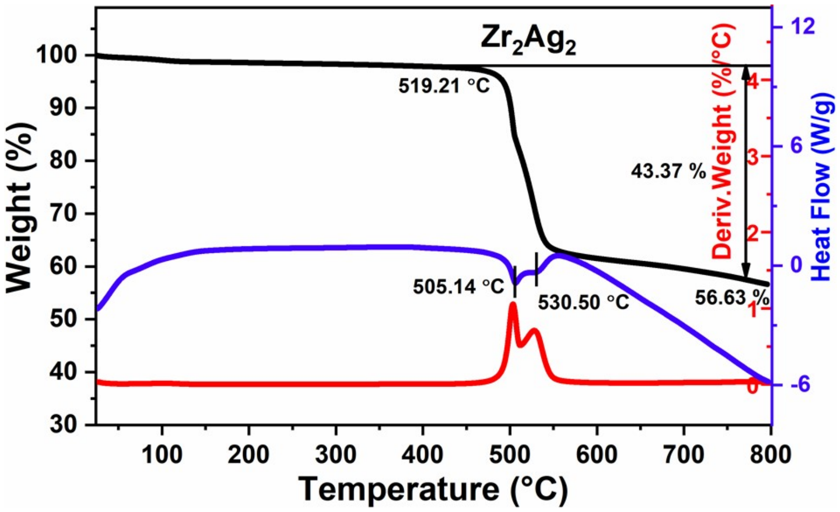

Figure S16. The TGA and DSC curves of **Zr$_2$Ag$_2$**.

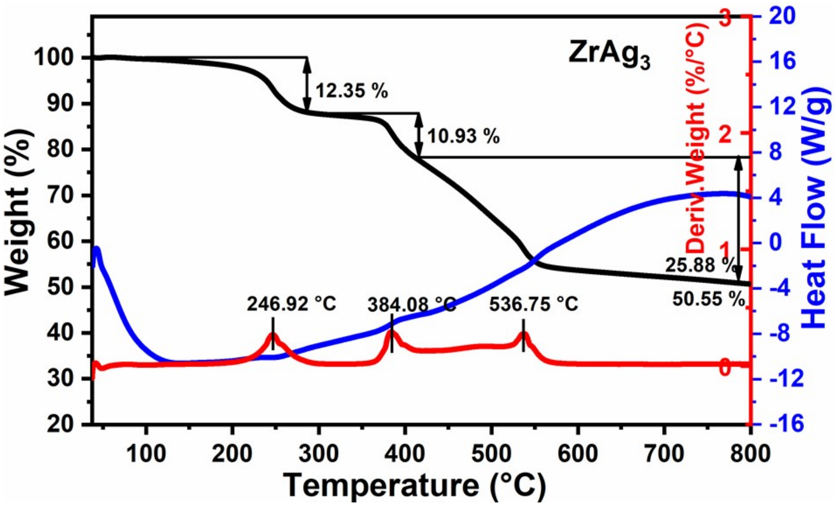

Figure S17. The TGA and DSC curves of **ZrAg$_3$**.

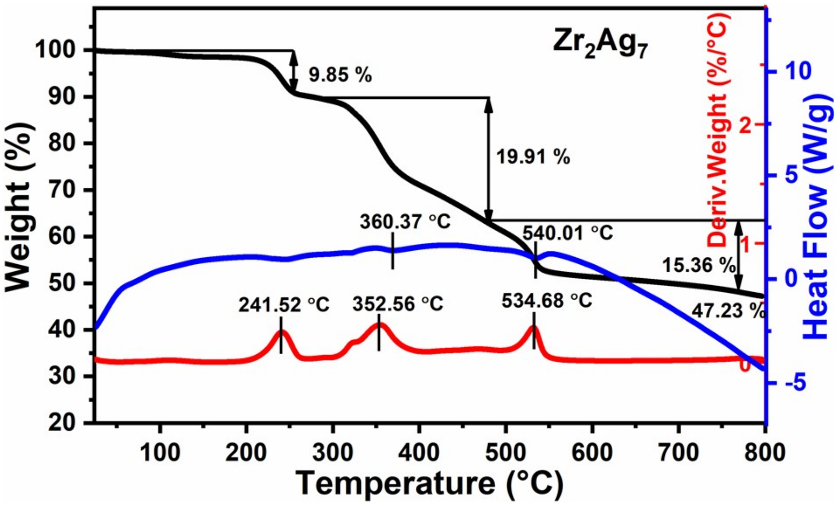

Figure S18. The TGA and DSC curves of **Zr$_2$Ag$_7$**.

6. XPS Analysis

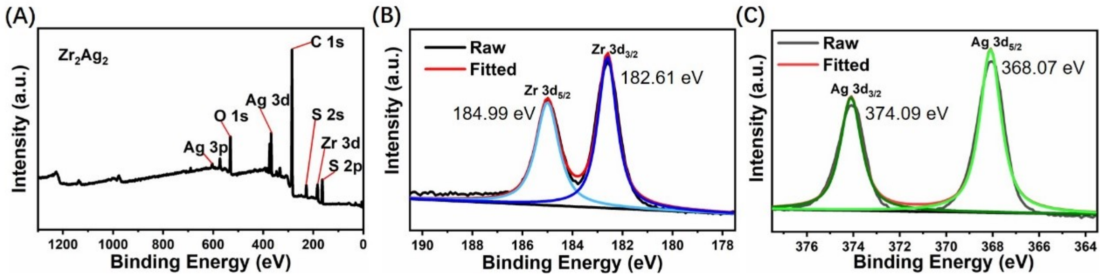

Figure S19. (A) XPS survey of **Zr$_2$Ag$_2$**. XPS survey of the **Zr$_2$Ag$_2$** showed the presence of Zr, Ag, S, C and O elements, consistent with the EDS mapping results; (B) High-resolution XPS spectra of Zr 3d in **Zr$_2$Ag$_2$**. The high-resolution Zr 3d spectrum shows two peaks at 184.99 and 182.61 eV that are assigned to the binding energy of Zr 3d$^{5/2}$ and Zr 3d$^{3/2}$ respectively; (C) High-resolution XPS spectra of Ag 3d in **Zr$_2$Ag$_2$**. The high-resolution Ag 3d spectrum shows two peaks at 374.09 and 368.07 eV that are assigned to the binding energy of Ag 3d$^{5/2}$ and Ag 3d$^{3/2}$ respectively.

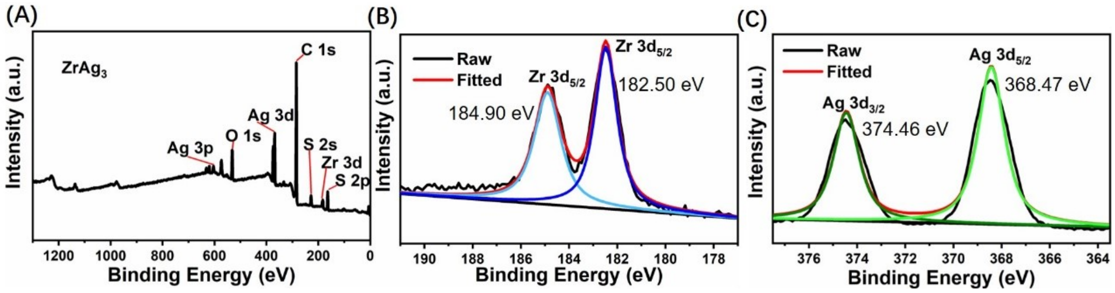

Figure S20. (A) XPS survey of **ZrAg$_3$**. XPS survey of the **ZrAg$_3$** showed the presence of Zr, Ag, S, C and O elements, consistent with the EDS mapping results; (B) High-resolution XPS spectra of Zr 3d in **ZrAg$_3$**. The high-resolution Zr 3d spectrum shows two peaks at 184.90 and 182.50 eV that are assigned to the binding energy of Zr $3d^{5/2}$ and Zr $3d^{3/2}$ respectively; (C) High-resolution XPS spectra of Ag 3d in **ZrAg$_3$**. The high-resolution Ag 3d spectrum shows two peaks at 374.46 and 368.47 eV that are assigned to the binding energy of Ag $3d^{5/2}$ and Ag $3d^{3/2}$ respectively.

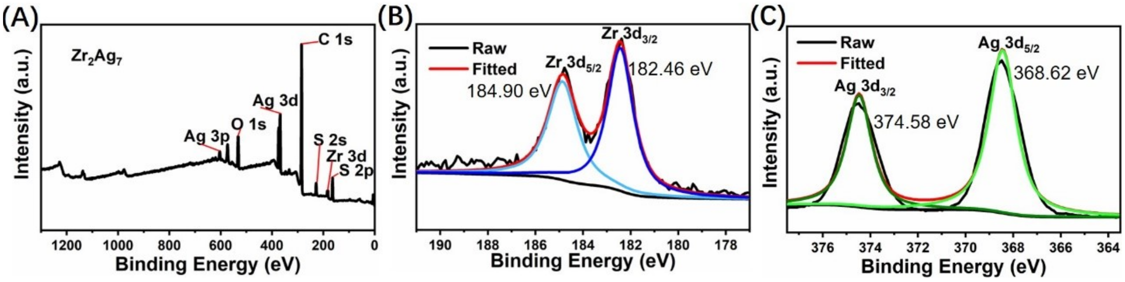

Figure S21. (A) XPS survey of **Zr$_2$Ag$_7$**. XPS survey of the **Zr$_2$Ag$_7$** showed the presence of Zr, Ag, S, C and O elements, consistent with the EDS mapping results; (B) High-resolution XPS spectra of Zr 3d in **Zr$_2$Ag$_7$**. The high-resolution Zr 3d spectrum shows two peaks at 184.90 and 182.46 eV that are assigned to the binding energy of Zr $3d^{5/2}$ and Zr $3d^{3/2}$ respectively; (C) High-resolution XPS spectra of Ag 3d in **Zr$_2$Ag$_7$**. The high-resolution Ag 3d spectrum shows two peaks at 374.58 and 368.62 eV that are assigned to the binding energy of Ag $3d^{5/2}$ and Ag $3d^{3/2}$ respectively.

7. SEM and EDX analysis

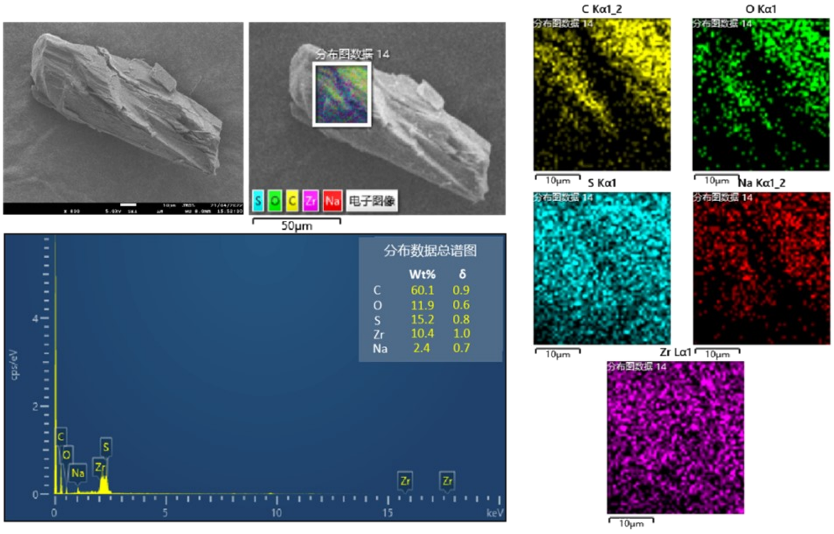

分布数据总谱图

	Wt%	δ
C	60.1	0.9
O	11.9	0.6
S	15.2	0.8
Zr	10.4	1.0
Na	2.4	0.7

Figure S22. SEM and EDX of **Zr$_2$Na$_2$**.

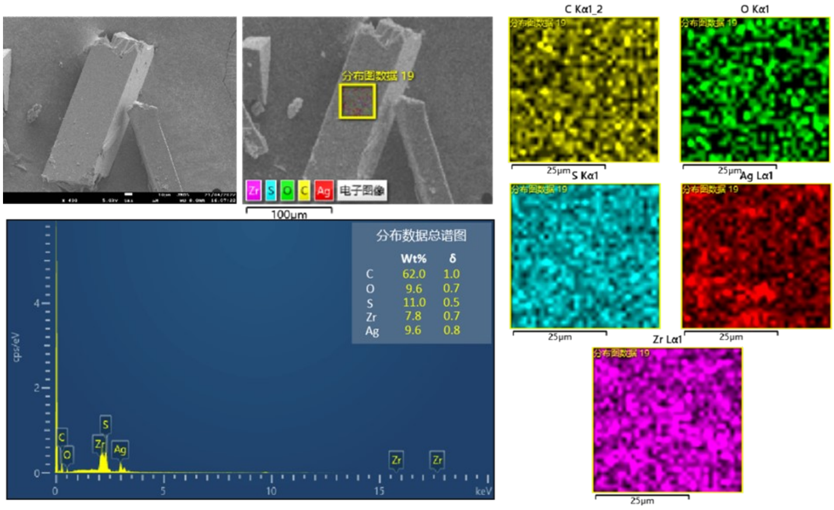

分布数据总谱图

	Wt%	δ
C	62.0	1.0
O	9.6	0.7
S	11.0	0.5
Zr	7.8	0.7
Ag	9.6	0.8

Figure S23. SEM and EDX of **Zr_2Ag_2**.

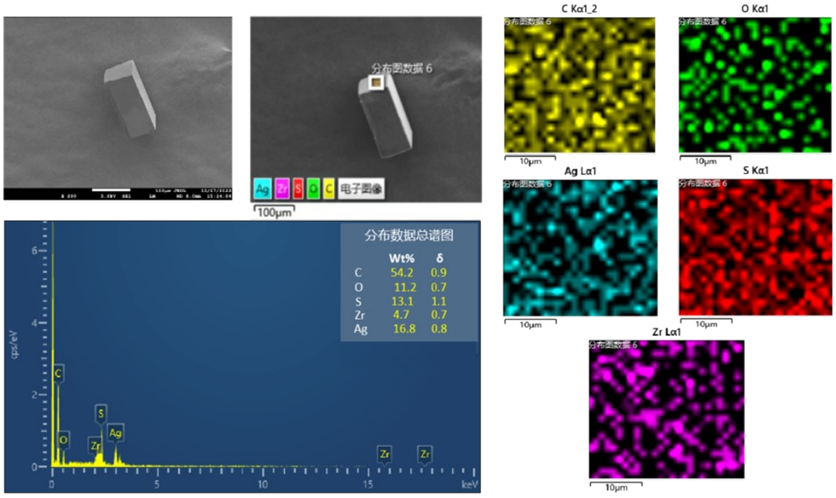

分布数据总谱图

	Wt%	δ
C	54.2	0.9
O	11.2	0.7
S	13.1	1.1
Zr	4.7	0.7
Ag	16.8	0.8

Figure S24. SEM and EDX of **$ZrAg_3$**.

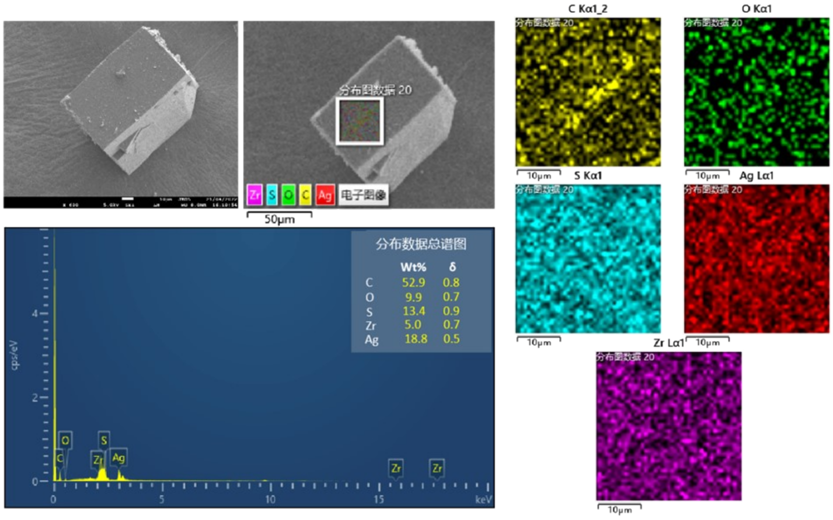

分布数据总谱图

	Wt%	δ
C	52.9	0.8
O	9.9	0.7
S	13.4	0.9
Zr	5.0	0.7
Ag	18.8	0.5

Figure S25. SEM and EDX of **Zr_2Ag_7**.

8. ESI-MS Analysis

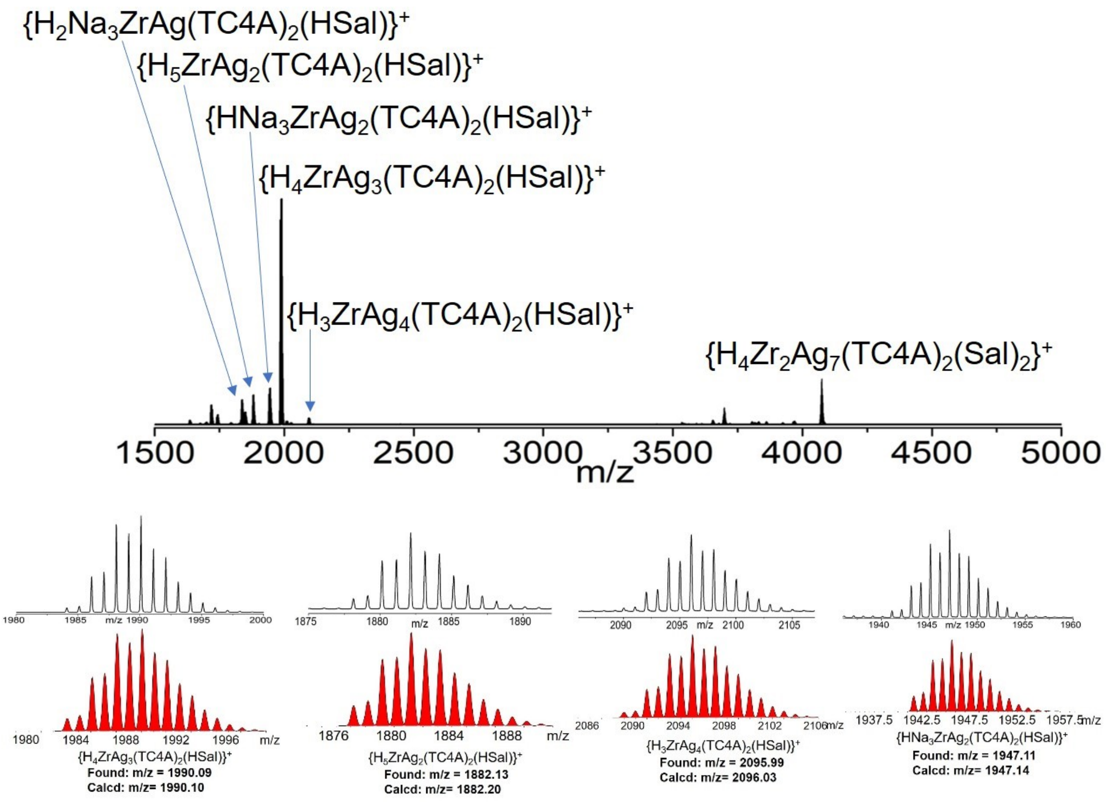

Figure S26. ESI-MS of $\mathbf{Zr_2Ag_7}$ in CH_2Cl_2.

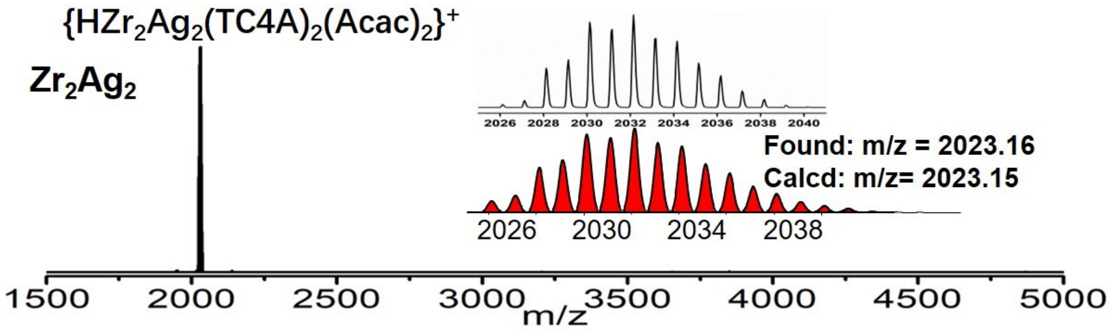

Figure S27. ESI-MS of $\mathbf{Zr_2Ag_2}$ in CH_2Cl_2.

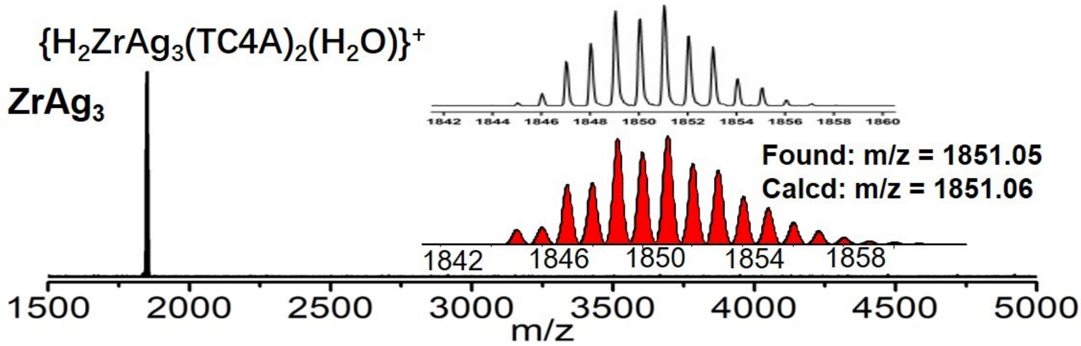

Figure S28. ESI-MS of $\mathbf{ZrAg_3}$ in CH_2Cl_2.

12.Electrocatalytic CO_2 reduction

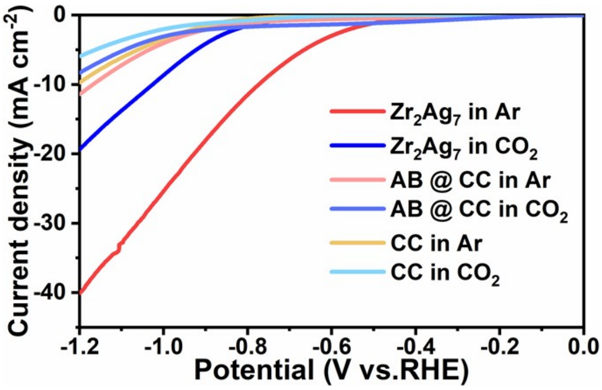

Figure S29. LSV of Zr^2Ag^7, blank carbon cloth (CC) and acetylene black coated carbon cloth (AB@CC) in Ar or CO_2 saturated 0.5 M $KHCO_3$ solution.

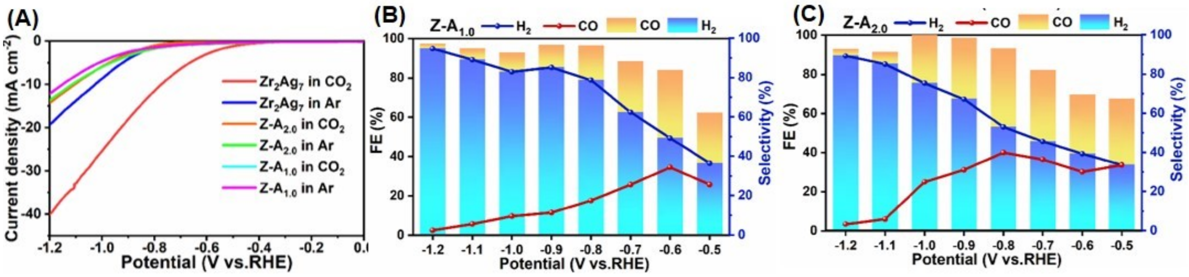

Figure S30. (A) LSV of **Zr_2Ag_7**, **Z-$A_{1.0}$** and **Z-$A_{2.0}$** in Ar or CO_2 saturated 0.5 M $KHCO_3$ solution; Faraday efficiency and selectivity of **Z-$A_{1.0}$**(B) and **Z-$A_{2.0}$**(C).

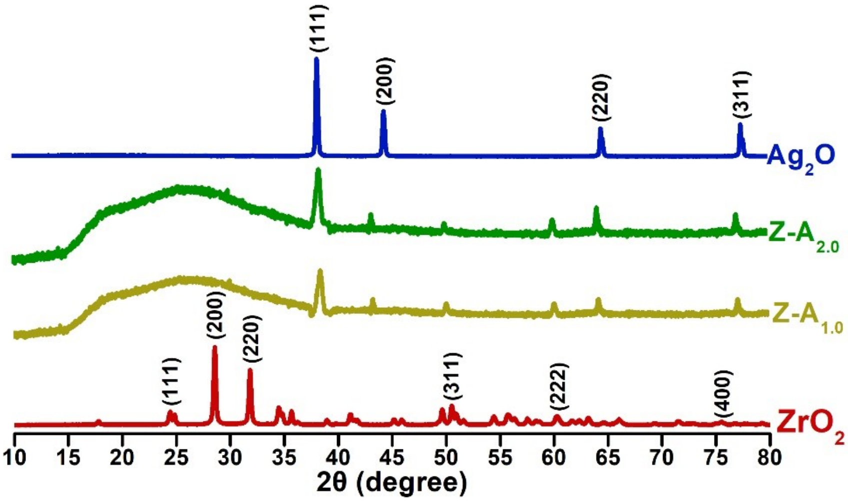

Figure S31. X-ray diffraction (XRD) patterns of ZrO_2, Ag_2O, and Z-A samples.

The synthesis method of ZrO_2-Ag_2O is as follows: ZrO_2-Ag_2O nanoparticles were made using sol-gel method as described by literature. "Zirconium butoxide (3.658 mL) was mixed with acetic acid (10 mL) and was later hydrolyzed with water (20 mL) dropwise. Within 15 minutes, a sol was formed. Followed by the addition of an aqueous solution of 1M or 2M (both 3.658mL in volume) $AgNO_3$ to the above sol with nonstop stirring to the above sol for the preparation of Z-A1.0 and Z-A1.0, respectively. Powder was obtained when the sol was placed in an oven at 80°C for gelation and then dried at 100°C. ZrO2-Ag_2O nanoparticles were obtained when the powders were processed and calcinated at 500°C for 4 hours.

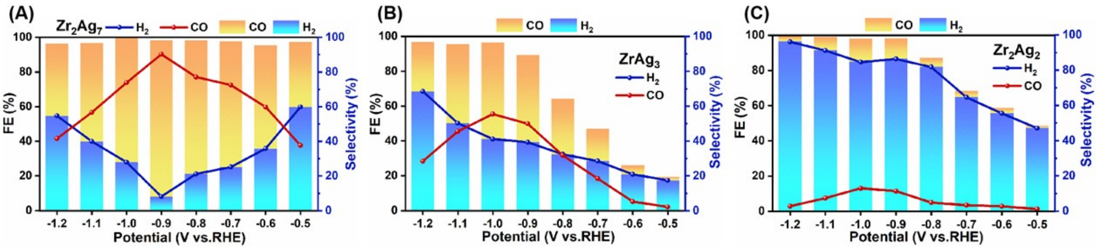

Figure S32. FEs and selectivities for CO and H_2 at potentials of -0.5 and -1.2 V over **Zr_2Ag_7**, **$ZrAg_3$** and **Zr_2Ag_2**, respectively.

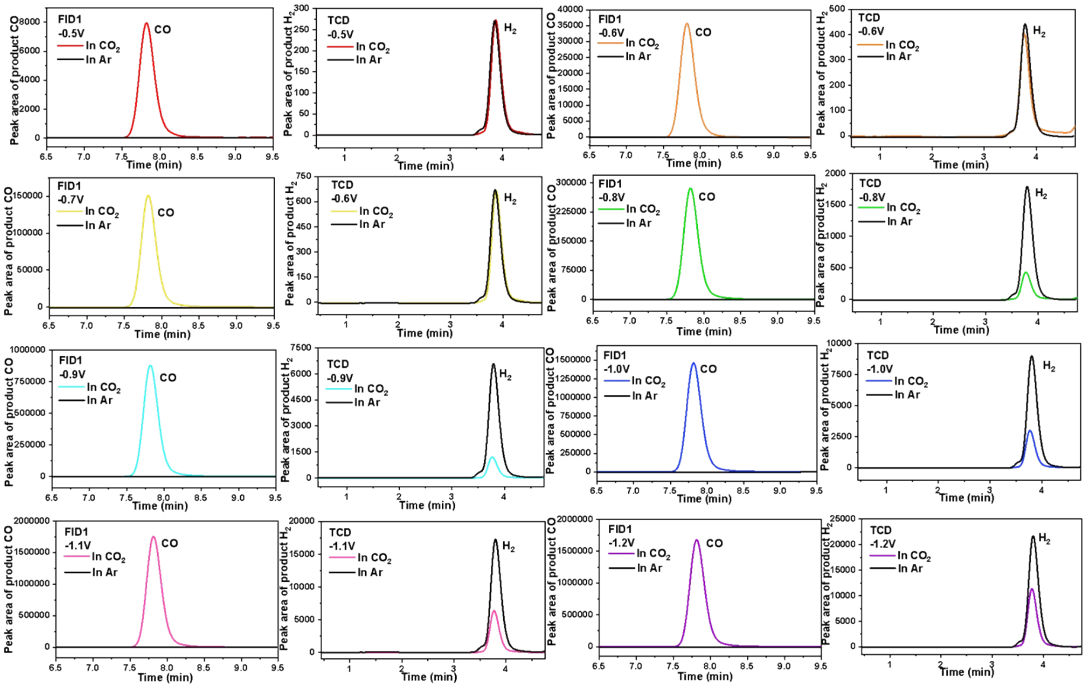

Figure S33. Gas chromatogram spectra of the CO and H_2 products signal measured at different voltage vs. RHE from eCO_2RR by using **Zr_2Ag_7** as electrocatalyst in Ar or CO_2.

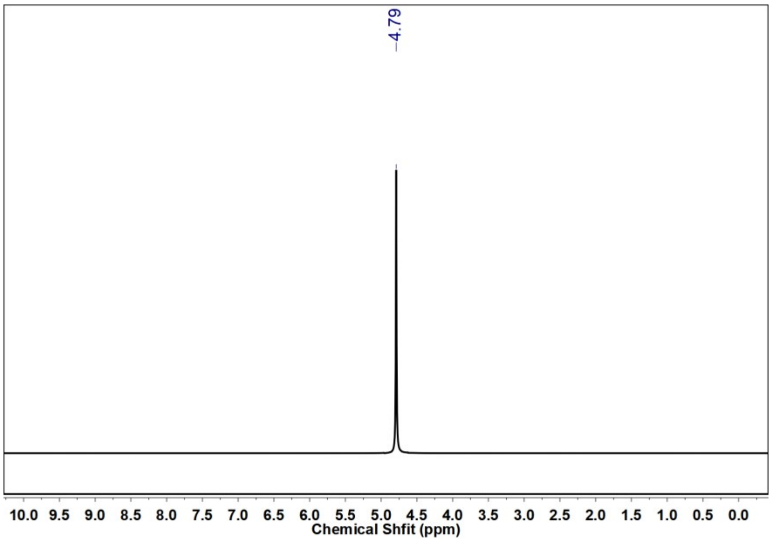

Figure S34. ^{1}H NMR spectrum of electrolyte solution in D_2O after eCO_2RR.

Table S2. Comparison of the electrocatalytic performances of Ag-based electrocatalysts for CO_2RR.

Catalyst	**Application potential**	**Electrolyte**	**FE_{CO} (%)**	**Reference**
Ti_8Ag_8	-0.9 V (vs. RHE)	1.0 M $KHCO_3$	92.4	S1
Ag_{30}	-0.9 V (vs. RHE)	1.0 M $KHCO_3$	93.4	S2
Ag-EPy-2	-0.7 V (vs. RHE)	0.1 M $KHCO_3$	74.0	S3
$Ag_{49}Mo_{16}$	-0.8 V (vs. RHE)	0.5 M $KHCO_3$	44.75	S4
Ag@UiO-66-SH	-1.1 V (vs. RHE)	0.1 M $KHCO_3$	74.0	S5
Ag_{15}	-0.6 V (vs. RHE)	0.5 M $KHCO_3$	95.0	S6
$Ag_{15}Cu_6$	-0.81 V (vs. RHE)	0.1 M $KHCO_3$	91.3	S7
Mo_2Ag_{12}	-0.8 V (vs. RHE)	0.5 M $KHCO_3$	60.85	S8
Ag_2Ti_{12}	-0.8 V (vs. RHE)	0.1 M $KHCO_3$	29.4	S9
Zr_2Ag_7	-0.9 V (vs. RHE)	0.5 M $KHCO_3$	90.23	This work

The relevant references are as follows:

S1. Y-Q. Tian, W-L. Mu, L-L. Wu, X-Y. Yi, J. Yan and C. Liu, Stepwise assembly of thiacalix[4]arene-protected Ag/Ti bimetallic nanoclusters: Accurate identification of catalytic Ag sites in CO_2 electroreduction, *Chemical Science*, 2023, 14, 10212-10218.

S2. L. J. Li, Y. T. Luo, Y. Q. Tian, P. Wang, X. Y. Yi, J. Yan, Y. Pei and C. Liu, *Inorg. Chem.*, 2023, **62**, 14377-14384.

S3. M. Abdinejad, E. Irtem, A. Farzi, M. Sassenburg, S. Subramanian, H. P. I. van Montfort, D. Ripepi, M. R. Li, J. Middelkoop, A. Seifitokaldani and T. Burdyny, *ACS Catal.*, 2022, **12**, 7862-7876.

S4. S. Q. Li, L. F. Dai, Y. Q. Tian, X, Y, Yi, J. Yan and C. Liu, *Chem. Commun.*, 2023, **59**, 576-578.

S5. R. K. Aparna, V. Surendran, D. Roy, B. Pathak, M. M. Shaijumon and S. Mandal, *ACS Appl. Energy Mater.*, 2023, **6**, 4072-4078.

S6. L. B. Qin, F. Sun, X. S. Ma, G. Y. Ma, Y. Tang, L. K. Wang, Q. Tang, R. C. Jin and Z. H. Tang, *Angew. Chem. Int. Ed.*, 2021, **60**, 26136-26141.

S7. G. C. Deng, J. M. Kim, M. S. Bootharaju, F. Sun, K. Lee, Q. Tang, Y. J. Hwang and T. Hyeon, *J. Am. Chem. Soc.*, 2023, **145**, 3401-3407.

S8. S. Q. Li, L. J. Li, Y. Q. Tian, W. L. Mu, R. X. Meng, J. Yan and C. Liu, *Polyoxometalates*, 2024, **3**, 9140038.

S9. Y. J. Liu, P. Shao, M. Y. Gao, W. H. Fang and J. Zhang, *Inorg. Chem.*, 2020, **59**, 11442-11448.

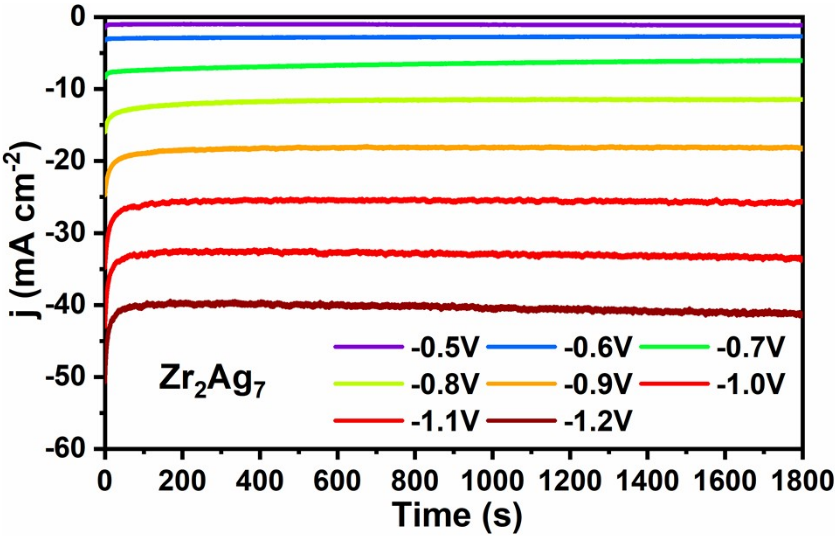

Figure S35. I-t test of **Zr_2Ag_7** catalyst under different voltage.

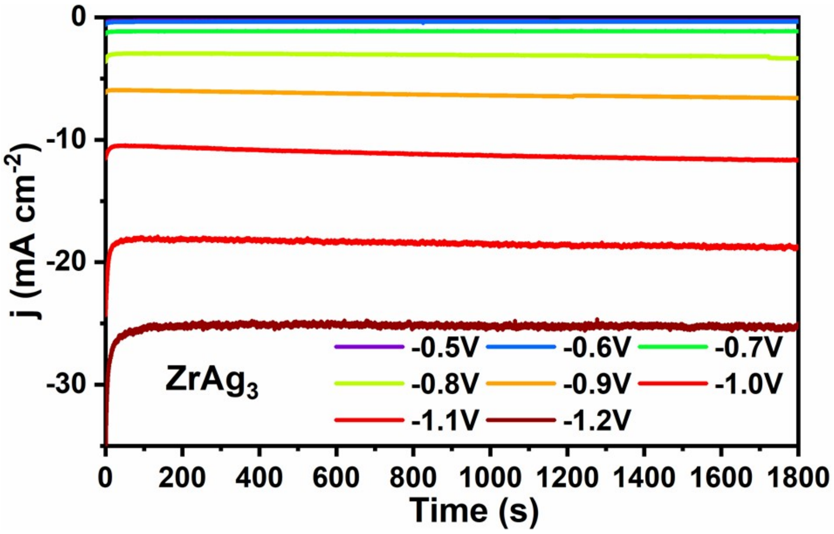

Figure S36. I-t test of **$ZrAg_3$** catalyst under different voltage.

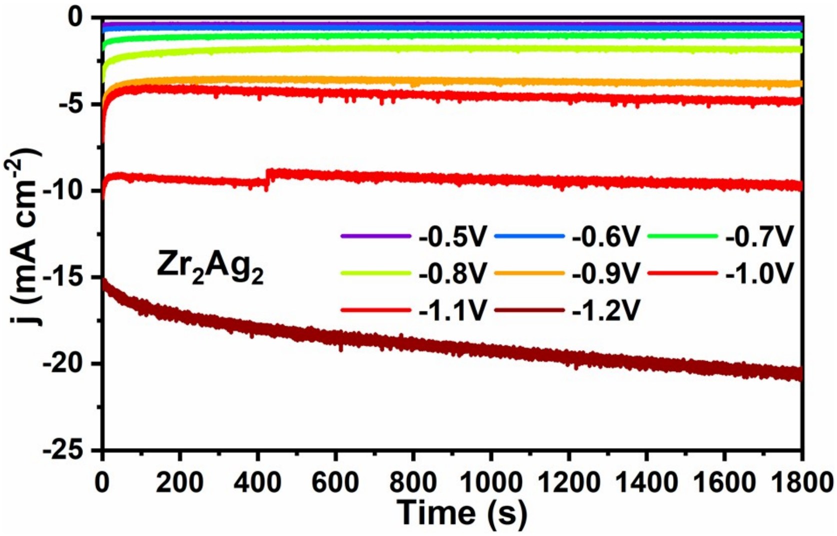

Figure S37. I-t test of **Zr_2Ag_2** catalyst under different voltage.

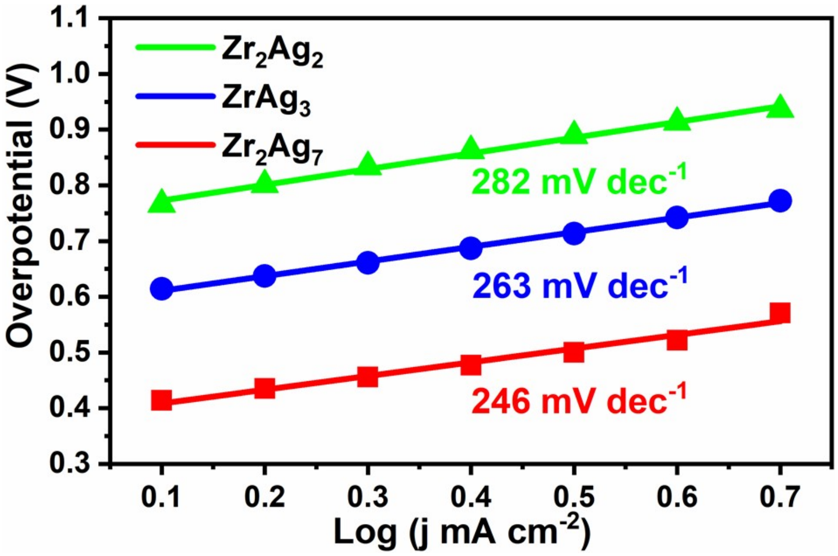

Figure S38. Tafel slopes of **Zr_2Ag_7, $ZrAg_3$** and **Zr_2Ag_2**.

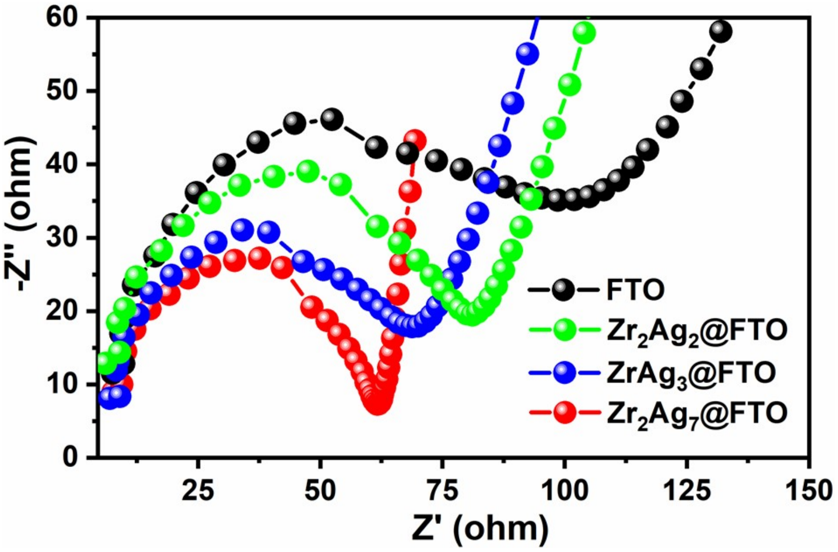

Figure S39. EIS of **Zr_2Ag_7**, **$ZrAg_3$** and **Zr_2Ag_2**.

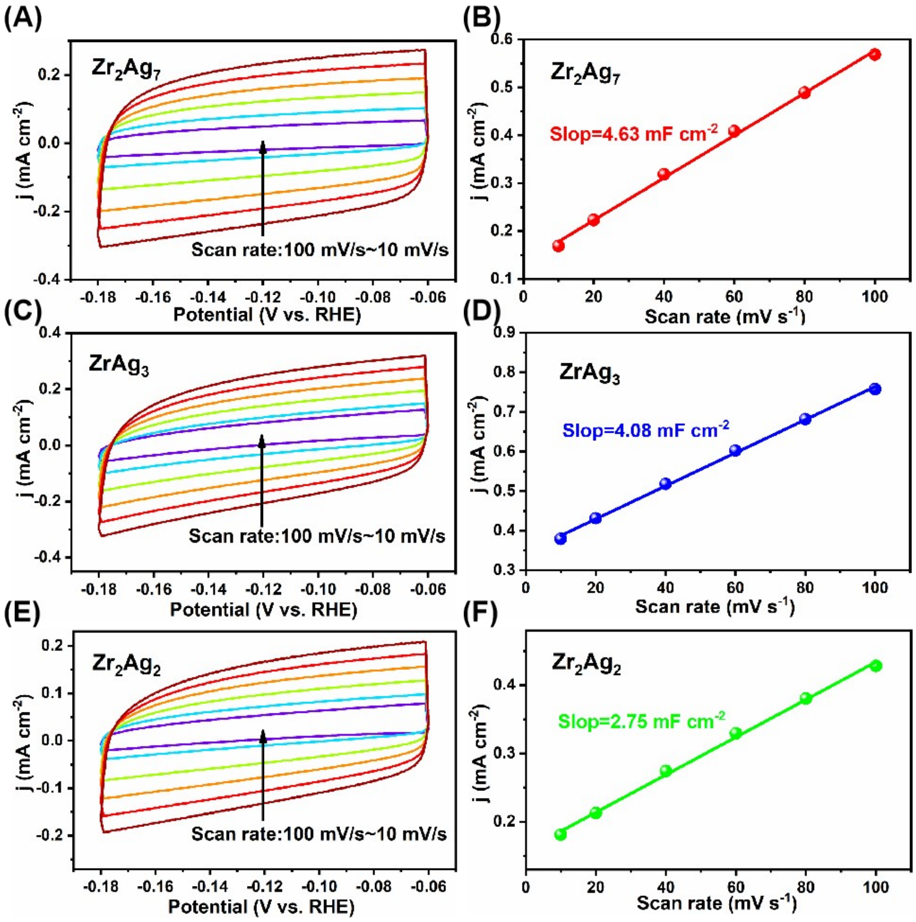

Figure S40. (A) The CV measurements with various scan rates for **Zr_2Ag_7** in CO_2-saturated 0.5 M $KHCO_3$ electrolyte; (B) The capacitive current density ($J_a/2-J_c/2$) as a function of scan rate of **Zr_2Ag_7**; (C) The CV measurements with various scan rates for **$ZrAg_3$** in CO_2-saturated 0.5 M $KHCO_3$ electrolyte; (D) The capacitive current density ($J_a/2-J_c/2$) as a function of scan rate of **$ZrAg_3$**; (E) The CV measurements with various scan rates for **Zr_2Ag_2** in CO_2-saturated 0.5 M $KHCO_3$ electrolyte; (F) The capacitive current density ($J_a/2-J_c/2$) as a function of scan rate of **Zr_2Ag_2**.

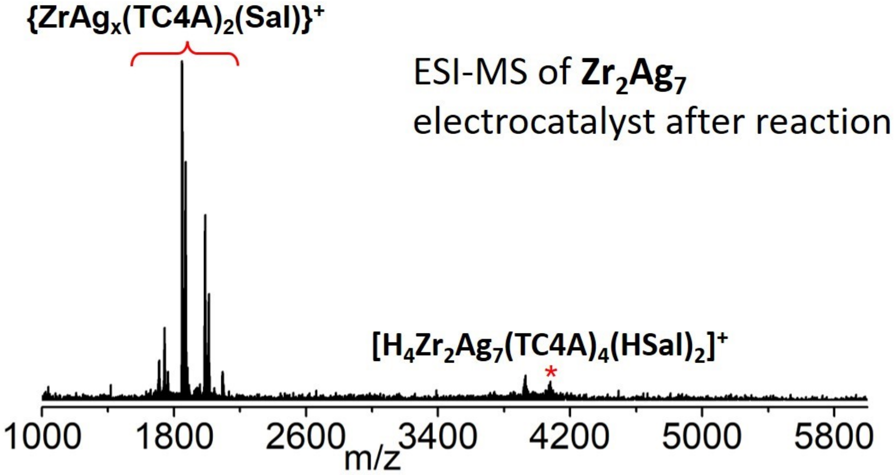

Figure S41. ESI-MS of **Zr_2Ag_7** electrocatalysts after reaction.

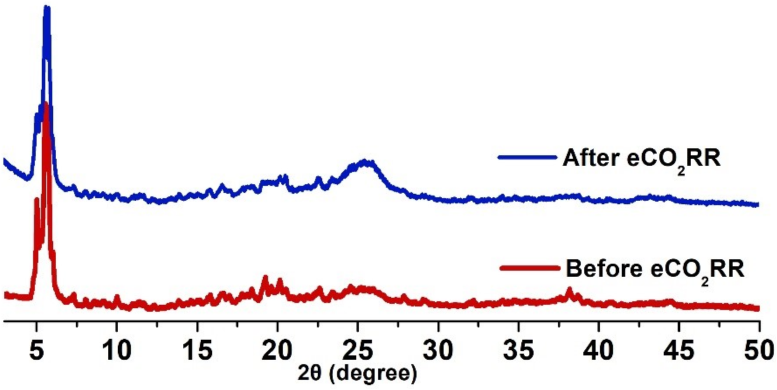

Figure S42. The XRD patterns of **Zr_2Ag_7** before and after electrocatalytic reaction.

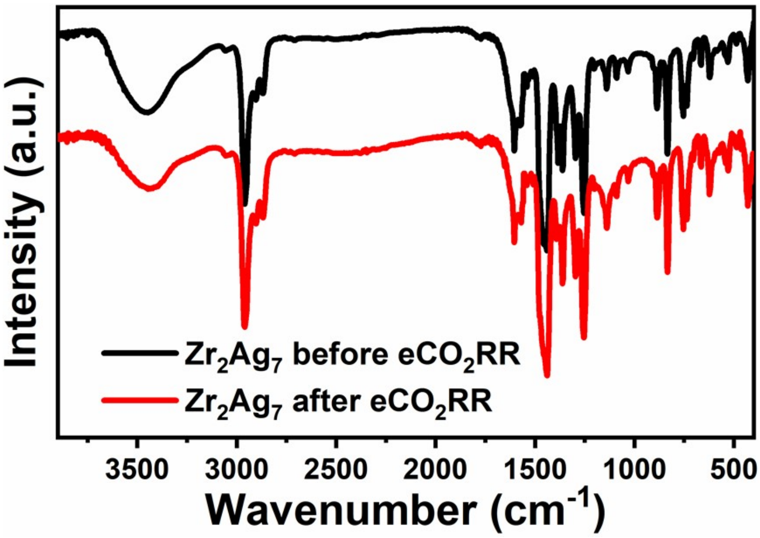

Figure S43. IR pattern of **Zr_2Ag_7** after electrocatalysis experiment.

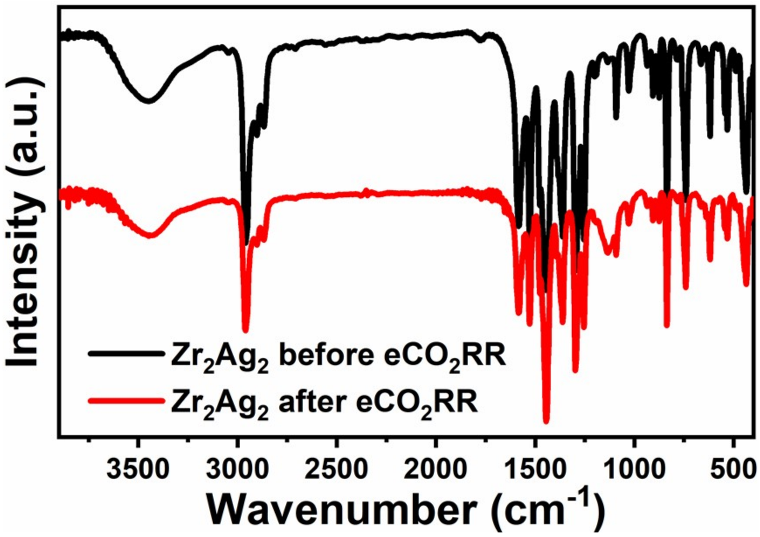

Figure S44. IR patterns of **Zr_2Ag_2** after electrocatalysis experiment.

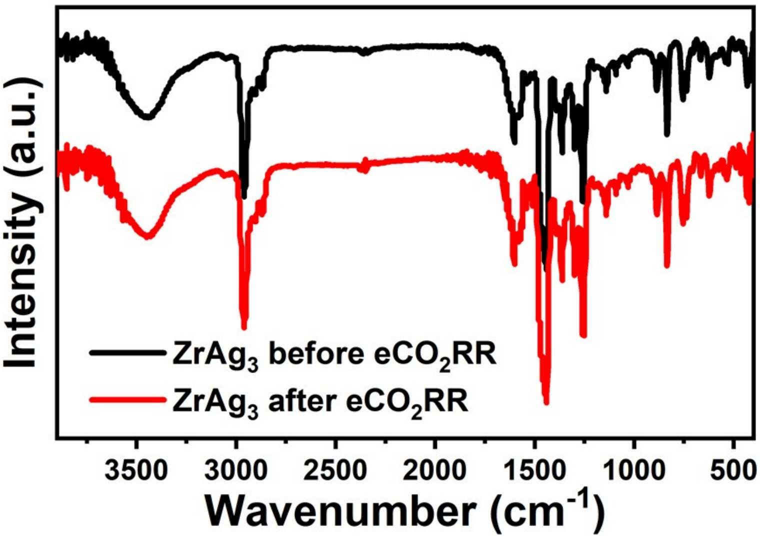

Figure S45. IR pattern of **$ZrAg_3$** after electrocatalysis experiment.

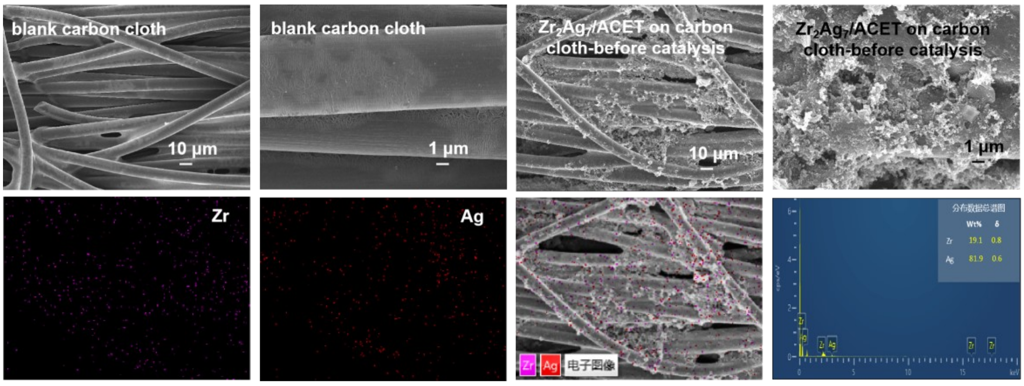

Figure S46. The EDS patterns of **Zr_2Ag_7**/ACET before electrocatalysis experiment.

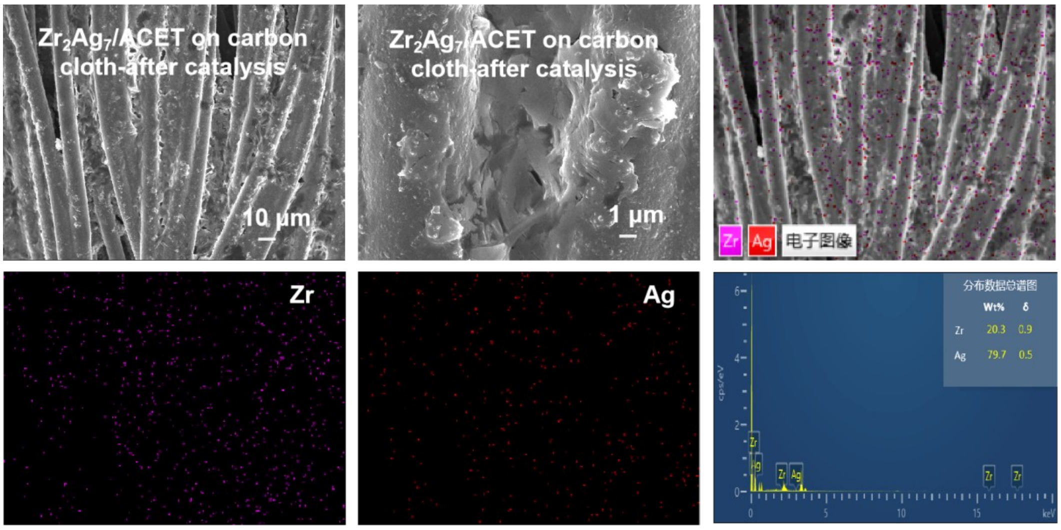

Figure S47. The EDS patterns of **Zr_2Ag_7**/ACET after electrocatalysis experiment.

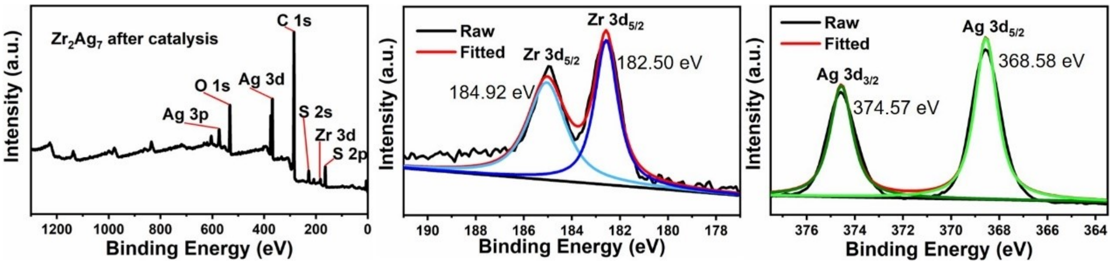

Figure S48. XPS survey of **Zr$_2$Ag$_7$** after electrocatalysis experiment. High-resolution XPS spectra of Ag 3d showed no significant change in the binding energy of the Ag in the catalyst before and after the reaction, indicating the preservation of its coordination environment in **Zr$_2$Ag$_7$** after electrocatalysis experiment.

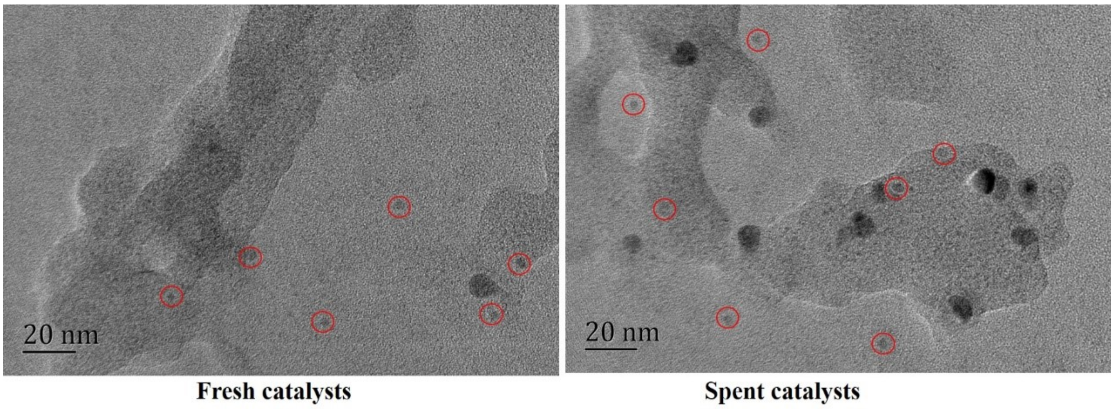

Figure S49. TEM image of **Zr$_2$Ag$_7$** electrocatalysts before and after reaction.

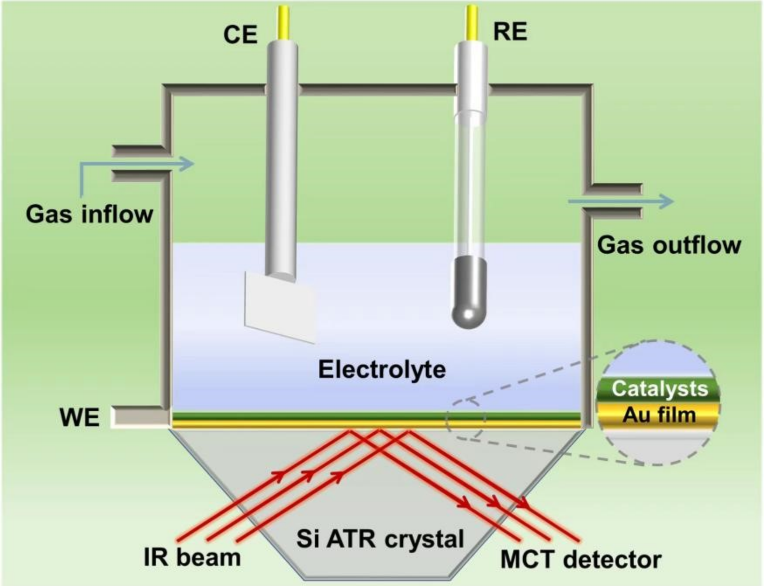

Figure S50. Schematic diagram of the in-situ attenuated total reflection FTIR (ATR-FTIR) on catalysts in electrolytes.

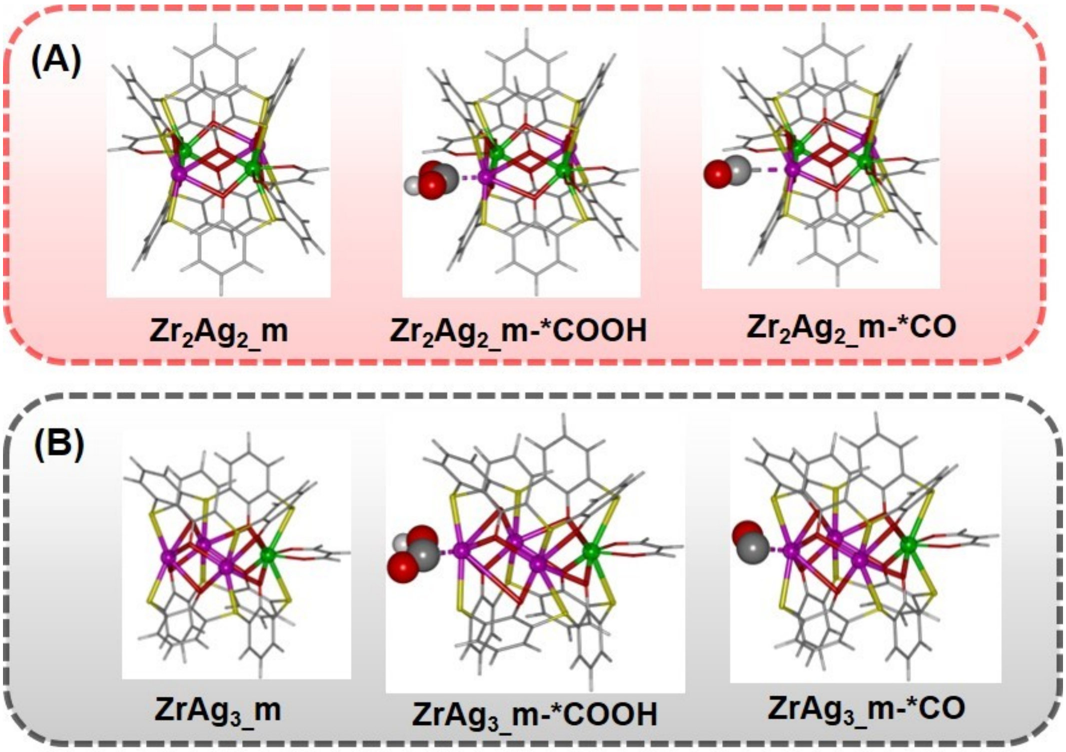

Figure S51. Optimized structural intermediates of *COOH and *CO for **Zr_2Ag_2_m** and **$ZrAg_3$_m.**